

Shell feature: a new radiomics descriptor for predicting distant failure after radiotherapy in non-small cell lung cancer and cervix cancer

Hongxia Hao^{1,2,3}, Zhiguo Zhou³, Shulong Li^{3,4}, Genevieve Maquilan³, Michael R. Folkert³, Puneeth Iyengar³, Kenneth D. Westover³, Kevin Albuquerque³, Fang Liu^{1,2}, Hak Choy³, Robert Timmerman³, Lin Yang⁵, Jing Wang³

1. School of Computer Science and Technology, Xidian University, Xi'an, 710071, China, 2. Key Laboratory of Intelligent Perception and Image Understanding of Ministry of Education, International Research Center for Intelligent Perception and Computation, Joint International Research Laboratory of Intelligent Perception and Computation, Xidian University, Xi'an, 710071, China, 3. Department of Radiation Oncology, University of Texas Southwestern Medical Center, Dallas, TX, 75235, United States, 4. School of Biomedical Engineering, Southern medical university, Guangzhou, 510515, China, 5. Department of Pathology, National Cancer Center/Cancer Hospital, Chinese Academy of Medical Sciences, Beijing, 100021, China.

Acknowledgement: This work was supported in part by the American Cancer Society (ACS-IRG-02-196) and US National Institutes of Health (5P30CA142543). The authors would like to thank Dr. Damiana Chiavolini for providing helpful suggestions and editing the manuscript.

Corresponding Author: Jing Wang, Associate Professor, Department of Radiation Oncology, UT Southwestern Medical Center, 2280 Inwood Rd. Dallas, TX, 75235-9303; e-mail: Jing.Wang@utsouthwestern.edu; Tel: 214-648-1795; fax: 214-645-2885.

Running head: Shell Feature for Predicting Distant Failure in NSCLC and CC

Disclaimers: The authors declare that they have no conflict of interest.

ABSTRACT

Purpose

To develop and demonstrate a novel tumor shell feature for predicting distant failure in non-small cell lung cancer (NSCLC) and cervical cancer (CC) patients.

Patients and Methods

The shell predictive model was constructed using pre-treatment positron emission tomography (PET) images from 48 NSCLC patients received stereotactic body radiation therapy (SBRT) and 52 CC patients underwent external beam radiation therapy and concurrent chemotherapy followed with high-dose-rate intracavitary brachytherapy. A shell feature, consisting of outer voxels around the tumor boundary, was extracted from a series of axial PET slices. The hypothesis behind this feature is that non-invasive and invasive tumors may have different morphologic patterns in the tumor periphery, in turn reflecting the differences in radiological presentations in the PET images. The shell's utility was evaluated by the support vector machine (SVM) classifier in comparison with intensity, geometry, gray level co-occurrence matrix (GLCM)-based texture, neighborhood gray tone difference matrix (NGTDM)-based texture, and a combination of these four features. The results were assessed in terms of accuracy, sensitivity, specificity, and the area under the receiver operating curve (AUC).

Results

For NSCLC, the AUC achieved by the shell feature was 0.82 while the highest AUC achieved by the other features was 0.76. Similarly, for CC, the AUC achieved by the shell feature was 0.83 while the highest AUC achieved by the other features was 0.76. Also, the difference in performance between shell and the other features was significant ($P < 0.005$) in all cases.

Conclusions

We propose a boundary-based shell feature that correlates with tumor metastasis. The shell feature showed better predictive performance than all the other features for distant failure prediction in both NSCLC and CC.

INTRODUCTION

Distant failure occurs when malignant tumor cells metastasize to distant organs,^{1,2} causing up to 90% human cancers-associated deaths.^{3,4} Stereotactic body radiation therapy (SBRT) is widely used in patients with early stage medically inoperable non-small cell lung cancer (NSCLC), achieving 85-95% local control rates⁵⁻⁷. Despite the high local control rates, distant failure is still common, with 3-year and 5-year distant relapse rates of 22% and 31%, respectively.⁸⁻¹⁰ Similarly, in patients with locally advanced cervical cancer (CC), even receiving external beam radiation therapy (EBRT) with concurrent chemotherapy and intracavitary brachytherapy (ICBT) as the recommended therapy,¹¹ at least 20% of them still develop distant metastases;^{12,13} and in the patients with positive para-aortic involvement, the rate is more than 40%.^{14,15} Therefore, predicting distant failure in high risk patients is essential to achieve better treatment outcomes with intensified treatment modalities.

Although many of the mechanisms that govern metastasis are still unclear, the tumor microenvironment is known to regulate tumor evolution toward metastasis,^{16,17} as shown for cervix,^{18,19} lung,^{20,21} colon cancer among other cancer types.^{22,23}

A correlation was found between the microenvironment and distant failure,²⁴ typically exemplified by the theory of epithelial-to-

mesenchymal transition (EMT). In this process, a portion of cancer cells located at the tumor edges may acquire cancer stem cell (CSC)-like traits typical of metastasis, including self-renewal, tumor-originating, invasiveness, and elevated apoptosis resistance; these cancer cells depart from the main tumor and initiate metastasis, leading to junctional alterations and spatial heterogeneity.²⁵⁻²⁸ This cellular invasion process was simulated by a hybrid multiscale mathematical model, showing that invasive tumor cells first developed within the tumor and later penetrated the tumor edge to form metastases.²⁹

In addition to EMT and CSCs, tumor budding³⁰ is another factor contributing to invasion and correlating with worse outcomes in colon cancer,^{22,31,32} lung cancer,³³⁻³⁶ cervix cancer³⁷ among others.³⁸⁻⁴¹ In tumor budding, isolated or clustered small malignant cells are close to the tumor edge. Literature reviews have reported that tumor buds can be a realization of CSC and an exhibition of the EMT process,^{42,43} suggesting tumor budding as an independent prognostic factor.^{37,44,45}

Tumor islands were also observed on tumor edges.⁴⁶ In lung cancer, tumor islands are large nests of malignant cells connected with one another and with primary tumors in alveolar spaces, slightly near the tumor border; they also have been associated with poor prognosis.⁴⁷ Studies were expanded by discovering spread through air space (STAS), a phenomenon of aggressive cells within air spaces

closely beyond the edge of the tumor. STAS has been recognized an important pattern of invasion,⁴⁸⁻⁵⁰ and was approved by the 2015 World Health Organization as an independent metastatic predictor of lung cancer within the lung classification system.⁵¹

These findings suggest that the appearance of the interface between tumor and normal tissue may provide phenotypic information related to metastatic potential that would enable the development of prognostic and predictive models. This application is enabled by radiomics, which can extract quantitative radiologic imaging features related to the aforesaid cellular phenotype, i.e., EMT-induced CSC changes, tumor budding, tumor islands, and STAS.⁵² Furthermore, because of its potential correlation with pathologic morphology,⁵³⁻⁵⁶ positron emission tomography (PET) has been studied to predict the pathologic outcome of therapy in various cancers, including lung,⁵⁷⁻⁶⁰ cervix,^{61,62} and other cancers.⁶³⁻⁶⁵ These studies have revealed PET as a promising quantitative reflection of the pathologic heterogeneity at the tumor edges.

We developed the tumor shell, a radiomics feature that characterizes the tumor periphery and its correlation with distant failure. We demonstrated its ability in predicting treatment response for patients receiving SBRT for early stage NSCLC and for patients receiving EBRT and concurrent chemotherapy followed by high-dose-rate ICBT in stage IB-IVA CC.

PATIENTS AND METHODS

Patients

Our study was conducted at our institution, on two cohorts of patients approved by Institutional Review Board: (1) 48 early stage IA and IB NSCLC patients treated with SBRT from 2006 to 2012 (28 males and 20 females; mean age, 70.58 ± 9.84 years; range, 54 to 90 years); (2) 52 stage IB-IVA cervix cancer patients without para-aortic node involvement, treated with EBRT and concurrent chemotherapy followed by high-dose-rate ICBT from 2009 to 2012 (mean age, 47.10 ± 11.82 years; range, 26 to 72 years). In the NSCLC dataset, the total number of PET slices for each patient varied from 274 to 355, with 2.00 to 5.00-mm slice thickness and 4.0×4.0 -mm or 5.0×5.0 -mm pixel spatial resolution. Therefore, all slices were interpolated with the smallest slice thickness of 2.0 mm and spatial resolution of 4.0×4.0 mm to achieve a consistent format. In the CC dataset, all slices were used directly without interpolation since they had the same 5.00-mm slice thickness and 4.0×4.0 -mm pixel spatial resolution. Before tumor analysis, the raw

PET data were converted to standard uptake values (SUV).

Tumor Analysis

For each patient, slices containing primary tumors were selected for analysis. In the NSCLC cohort, tumors were segmented automatically, with the middle location slice segmented by the object information based interactive segmentation method (OIS)⁶⁶ and other slices segmented by the OTSU method.⁶⁷ In the CC cohort, the region of interest that incorporated the entire tumor was delineated manually by a radiation oncologist with 4 years' experience and reviewed by another radiation oncologist with 19 years' experience. In the NSCLC cohort, the number of selected slices originally ranged from 5 to 17, and zero padding was used for patients with slice numbers less than 17. Therefore, after interpolation to the smallest slice thickness of 2.0 mm, all patients had 42 slices. Meanwhile, because the greatest in-plane tumor diameter in all the patients' slices was 13 pixels, a patch of 17×17 pixels was cropped around the tumor center in each slice, resulting in a cube size of $17 \times 17 \times 42$ for each patient. A volume size of $29 \times 29 \times 40$ was used for each patient in the CC cohort. All features were computed on cropped PET cubes.

Tumor Shell Feature Construction

The shell feature was extracted from the voxels around the tumor boundaries in a series of axial PET slices. The workflow of the shell feature construction is illustrated in Fig 1. The top row shows slices of the tumor (outlined in the red windows) in axial sequence (Fig 1). As displayed in the second row (Fig 1), the patches that include the delineated tumor were cropped from the corresponding slices above and used to compute the shell feature. By thresholding the patches above zero, binary mask images were obtained to represent the specific tumor region. By using the mask images of every two adjacent patches, a number of difference images were derived. As expected, a difference image was generally the outer region of the tumor. By adding up the difference images, referred to as sub-shells in the third row in Fig 1, the shell feature was formed and used to represent the holistic heterogeneity of voxels in the boundary of the entire tumor volume.

The sub-shell sequence $\Psi(t)$ is defined as:

$$\Psi(t) = \begin{cases} (M(t) - M(t-1)) \circ (P(t) - P(t-1)), & t \geq 2 \\ \mathbf{0}, & t = 1 \end{cases} \quad (1)$$

where $P(t)$ denotes a patch sequence and $M(t)$ is the matching binary mask image sequence that indicates the region of the tumor, the symbol \circ indicates the

hadamard product and t is the patch (slice) number. When $t = 1$, $\Psi(t)$ is a zero matrix $\mathbf{0}$. The element in $\Psi(t)$ is either greater than (when corresponding elements in $M(t)$ and $M(t - 1)$ are 0, 1 or 1, 0) or equal to zero (when corresponding elements in $M(t)$ and $M(t - 1)$ are 0, 0 or 1, 1). Thus, each sub-shell partially describes the heterogeneous architecture of the tumor edge in an image where the higher SUV value pixels appear brighter. Examples of sub-shells are presented in Fig 1.

To represent the heterogeneity of the whole tumor border, for each patient k the shell feature $S(k)$ is constructed by successively accumulating sub-shells together and can be written as:

$$S(k) = \sum_{t=2}^n \Psi(t). \quad (2)$$

where n is the total slice amount with $n = 42$ in the NSCLC cohort and $n = 40$ in the CC cohort. The strength of the shell feature is the use of a compact, yet comprehensive description that captures a sequence of morphologic patterns across the tumor boundary, such as shape, size, SUV values, and heterogeneities in a simple 2D map (Fig 1, bottom row).

Handcrafted Feature

Our proposed shell feature was compared with the following five groups of handcrafted features: 9 intensity features, 8 geometry features, 12 second order gray level co-occurrence matrix (GLCM) features, 5 high order neighborhood gray tone difference matrix (NGTDM) texture features, and a combination of these four types, for a total of 34. The features are described in Table 2 and calculation functions are provided in the Supplement.

Prediction Model Development

To develop our prediction model we used a machine learning method based on support vector machine (SVM). SVM is a supervised learning model that can classify data through an optimal hyperplane representing the largest separation margin between two classes. Before being fed to SVM, the vectorized shell was applied by principal component analysis (PCA) to reduce the feature dimension. The reduction process is described in the Supplement. The predictive ability of the shell feature was compared with that of the other five features using ten random trails of 5-fold cross validation on both NSCLC and CC cohorts. Meanwhile, to handle the class imbalance problem, SVM was trained over preprocessed data by a synthetic minority over-sampling technique (SMOTE). Accuracy, sensitivity, specificity, and area under the receiver operating characteristic curve (AUC) were used as evaluation

metrics. The code was implemented in Matlab (version R2016a).

Statistical Analysis

The difference in AUC performance between the shell feature and the other features was assessed by the Student's t -test. The difference was considered statistically significant with a P value less than 0.05. The receiver operating characteristic (ROC) curve with 95% confidence interval is presented in Fig 2. Statistical analysis was performed with the Matlab statistical toolbox (version R2016a).

RESULTS

Clinical Characteristics

The demographic and clinical characteristics of patients in the NSCLC and CC cohorts are listed in Table 1. No significant difference in distant failure prevalence was observed between the two trials ($P = 0.917$). During follow-up time, distant metastases were observed in 25% (12 of 48) of patients in the NSCLC cohort and 26.9% (14 of 52) in the CC cohort after radiotherapy.

Comparison of Predictive Performance

The comparison between the shell feature and other features was performed on both NSCLC and CC cohorts through quantitative analysis (Table 3) and ROC graphing (Fig 2). AUC, sensitivity, specificity, and accuracy were the criteria used in the study. Definitions are given in the Supplement.

The shell feature showed the highest accuracy in predicting distant failure (Table 3). In the NSCLC cohort, the shell feature achieved an AUC of 0.82 (95% CI, 0.6632 to 0.9247) with 0.81 sensitivity, 0.80 specificity, and 0.81 accuracy. For the other five features, the best result was observed for the GLCM texture as shown by 0.76 AUC (95% CI, 0.5528 to 0.8905), 0.75 sensitivity, 0.74 specificity, and 0.75 accuracy. Similarly, in the CC cohort the shell feature still achieved the best performance for all metrics, with 0.83 AUC (95% CI, 0.6559 to 0.9212), 0.81 sensitivity, 0.80 specificity, and 0.80 accuracy. These results revealed that the shell feature had more discriminative capacity than the other features. Also, the difference in AUC performance between the shell feature and the other features was found to be significant ($P < 0.005$ for both features in both cohorts).

The ROC curves for different feature sets are illustrated in Fig 2. Similar results were obtained for NSCLC (Fig 2A) and CC (Fig 2B). The proposed shell feature, represented by the upper blue curve, is located close to the top left corner of the chart,

indicating on average a greater discriminative ability than the other methods.

The discriminative ability is indicated by representative 2D shell maps (Fig 3A and 3B) and vectorized shell feature matrixes (Fig 3C and 3D). The top row shows tumors without distant failure (Fig 3A) and the bottom row reports those with distant failure (Fig 3B). Pixels with higher SUV values are indicated in brighter colors, while lower values are shown in darker colors. As evident from the shell maps, distant failure-positive tumors show more heterogeneous boundary expression than the failure-negative ones. This finding may be attributed to the more active, varied, and potentially invasive cellular behavior of the tumor in the barrier microenvironment. The overall capability of the shell's classification for the NSCLC and CC cohorts is indicated in Fig 3C and 3D. The rows in the matrixes are the vectorized shell's sparse coefficients learned by the dictionary learning method.⁶⁸ Clustering characteristics can be seen on both cohorts, with features of the same class showing similar representation and features of different classes displaying distinct representations.

DISCUSSION

The potential of tumor boundary as a predictive factor for distant failure was evaluated by the tumor shell, a PET-derived feature that allows us to detect its associations with metastasis within the microenvironment. The shell feature can be used to predict the outcome of SBRT for NSCLC patients and EBRT and concurrent chemotherapy followed with high-dose-rate ICBT for CC patients.

The tumor-host interface has been associated with metastasis because interactions between tumor cells and their microenvironment play an active part in tumor invasion and metastasis.⁶⁹ However, to the best of our knowledge, few studies have targeted tumor boundaries in medical imaging for constructing risk models of metastasis.^{70,71} A recent study linked the morphology at the tumor-stroma interface to a multifractal metric, which derived from tumor outlines (excluding tumor internal tissue) on pathological images. The outline-based metric was found to be associated significantly ($P < 0.001$) with

metastasis-related features, such as tumor border configuration and tumor budding grade, thereby verifying its prognostic and predictive efficacy for treatment response in colon cancer.⁷⁰ Similarly, in a lung cancer review, a fractal dimension of the tumor-stroma interface was used to measure tumor progression.⁷¹ The study highlighted the use of radiological imaging, and found that the derived metric correlated with tumor growth and predicted treatment response.⁷¹ Notably, the predictors in these studies were scores calculated from the contour lines of the tumor edge, whereas our method used the areas of the tumor boundary, where more minable information may be included. Besides, the calculation of the scores is a handcrafted processing, which is subject to human inconsistency and operator dependence. By contrast, our shell feature uses the original image information of the tumor edge directly and eliminates any calculation or feature selection procedure, thereby may be more scalable and generalizable.

The correlation between distant failure and radiomics features of the tumor edge is based on known biological processes that are associated with metastatic potential such as EMT and tumor budding. On the assumption that these findings are located at the tumor boundary, the shell feature was proposed to describe spatial morphology of the tumor periphery in relation to the likelihood of metastasis. Moreover, to the extent that these processes are present in other tumor types, it is likely that the shell feature may be used to predict the outcomes for other cancers.

Our study presents a few limitations, including the use of a small patient population and a 5-fold cross validation instead of an independent validation cohort. Also, accumulating a serial of sub-shells (3D) into a 2D shell feature may lead to a loss of spatial complexity in the axial perspective. Finally, the influence of tumor boundary extension is not investigated in this paper.

In conclusion, the PET-derived shell feature revealed a relationship between tumor edge and distant failure, and can be used to facilitate early prediction of the radiotherapeutic response in NSCLC and CC patients.

TABLES & FIGURES

Table 1. Characteristics of two cohorts of patients				
Characteristics	NSCLC Cohort		CC Cohort	
	Distant failure (+)	Distant failure (-)	Distant failure (+)	Distant failure (-)
Age, years				
mean \pm SD	69.9 \pm 9.2	70.2 \pm 10.2	41.6 \pm 11.7	49.1 \pm 11.3
Median (range)	69.5 (57.0-89.0)	71.5 (54.0-90.0)	38.2 (29.3-70.9)	49.1 (26.2-72.0)
Ethnicity, No. (%)				
Caucasian	9 (75.0)	27 (75.0)	6 (42.9)	12 (31.6)
Hispanic	0 (0)	1 (1.3)	2 (14.3)	15 (39.5)
African American	3 (25.0)	7 (19.4)	5 (35.7)	10 (26.3)
Asian	0 (0)	1 (1.3)	1 (7.1)	0 (0)
Other	0 (0)	0 (0)	0 (0)	1 (2.6)
Clinical tumor size, mm, No. (%)				
\leq 10	1 (8.3)	0 (0)	0 (0)	1 (2.6)
11-30	6 (50.0)	26 (72.2)	2 (14.3)	4 (10.6)
31-50	5 (41.7)	9 (25.0)	9 (64.3)	20 (52.6)
51-70	0 (0)	1 (1.3)	2 (14.3)	9 (23.6)
$>$ 71	0 (0)	0 (0)	1 (7.1)	4 (10.6)
Histology, No. (%)				
Adenocarcinoma	6 (50.0)	17 (47.3)	1 (7.1)	4 (10.6)
Squamous cell carcinoma	5 (41.7)	12 (33.3)	11 (78.6)	33 (86.8)
Other	1 (8.3)	7 (19.4)	2 (14.3)	1 (2.6)
Stage, No. (%)				
IA	5 (41.7)	30 (83.3)	0 (0)	0 (0)
IB	7 (58.3)	6 (16.7)	4 (28.6)	12 (31.6)
IIA	0 (0)	0 (0)	1 (7.1)	3 (7.9)
IIB	0 (0)	0 (0)	7 (50.0)	15 (39.5)
IIIB	0 (0)	0 (0)	0 (0)	6 (15.8)
IVA	0 (0)	0 (0)	2 (14.3)	2 (5.2)

NOTE. Stages in NSCLC and CC are determined by the TNM and Federation of Gynecology and Obstetrics (FIGO) staging system, respectively. Abbreviations: NSCLC, non-small cell lung cancer; CC: cervix cancer; SD: standard deviation.

Table 2. Types of handcrafted features			
Histogrambased image intensity	Geometry	GLCM based texture	NGTDM based texture
Minimum	Volume	Energy	Coarseness
Maximum	Major diameter	Entropy	Contrast*
Mean	Minor diameter	Correlation	Busyness
Stand deviation	Eccentricity	Contrast*	Complexity
Sum	Elongation	Texture Variance	Texture Strength
Median	Orientation	Sum-Mean	
Skewness	Bounding Box Volume	Inertia	
Kurtosis	Perimeter	Cluster Shade	
Variance		Cluster tendency	
		Homogeneity	
		Max-Probability	
		Inverse Variance	

NOTE. *Contrast: Different calculation methods were employed in GLCM and NGTDM, though the same names are indicated. Abbreviations: GLCM, Gray level co-occurrence matrix; NGTDM, Neighborhood gray tone difference matrix.

Table 3. Prediction performance of features with respect to distant failure

cohort	features	Accuracy	Sensitivity	Specificity	AUC	95% CI	P value
NSCLC	Intensity	0.70 ± 0.01	0.70 ± 0.02	0.69 ± 0.01	0.73 ± 0.02	[0.5615,0.8613]	.0002
	Geometry	0.68 ± 0.01	0.65 ± 0.06	0.70 ± 0.04	0.65 ± 0.01	[0.4861,0.8009]	.0001
	GLCM texture	0.75 ± 0.03	0.75 ± 0.03	0.74 ± 0.03	0.76 ± 0.02	[0.5528,0.8905]	.0044
	NGTDM texture	0.68 ± 0.03	0.70 ± 0.06	0.65 ± 0.02	0.73 ± 0.03	[0.5139,0.8783]	.0015
	Combination	0.73 ± 0.04	0.72 ± 0.02	0.71 ± 0.03	0.76 ± 0.02	[0.5887,0.8796]	.0025
	Shell	0.81 ± 0.03	0.81 ± 0.02	0.80 ± 0.03	0.82 ± 0.03	[0.6632,0.9247]	–
CC	Intensity	0.72 ± 0.02	0.71 ± 0.03	0.75 ± 0.03	0.69 ± 0.01	[0.4743,0.8533]	.0003
	Geometry	0.71 ± 0.04	0.71 ± 0.01	0.71 ± 0.04	0.71 ± 0.01	[0.4891,0.8590]	.0006
	GLCM texture	0.75 ± 0.02	0.80 ± 0.02	0.73 ± 0.02	0.76 ± 0.04	[0.5427,0.8981]	.0015
	NGTDM texture	0.72 ± 0.04	0.71 ± 0.02	0.74 ± 0.04	0.74 ± 0.03	[0.5396,0.8524]	.0002
	Combination	0.72 ± 0.03	0.75 ± 0.05	0.73 ± 0.03	0.73 ± 0.02	[0.5519,0.8813]	< .0001
	Shell	0.80 ± 0.04	0.81 ± 0.02	0.80 ± 0.04	0.83 ± 0.02	[0.6559,0.9212]	–

NOTE. “Combination” refers to the combined four types of features, i.e., intensity, geometry, GLCM texture and NGTDM texture; 95% CI and P value are both derived from values of AUC; P value measures the statistical AUC difference between each group of handcrafted features and shell feature.

Abbreviations: AUC, the area under a characteristic operation curve; CI, confidence interval.

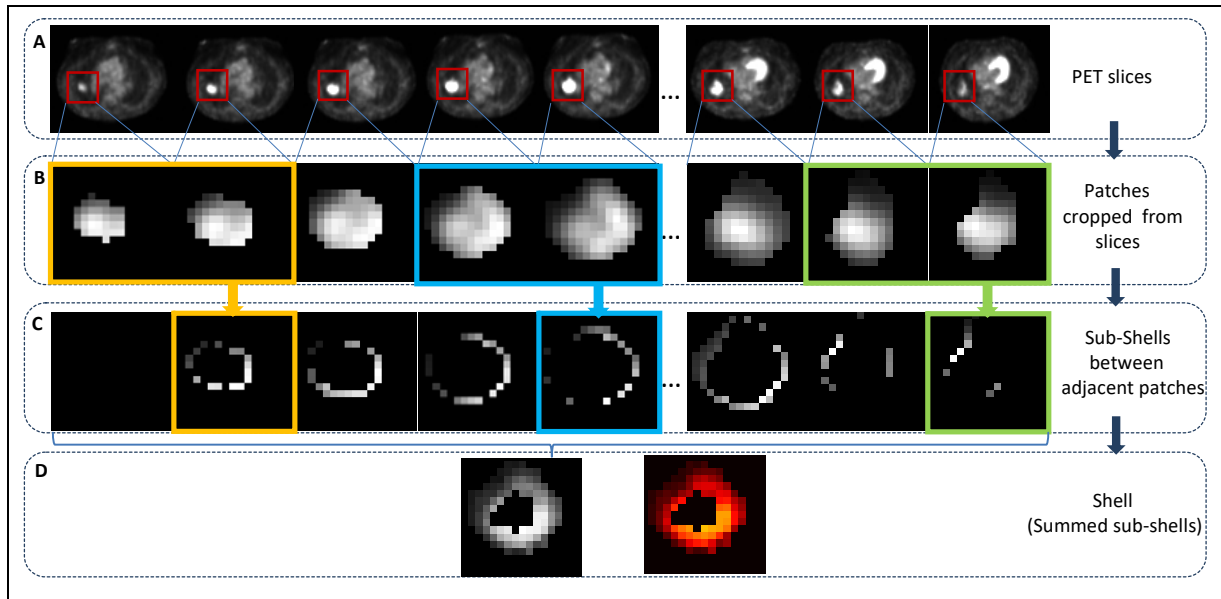


Fig 1. Shell feature extraction workflow. (A) Series of axial PET slices of one patient. (B) Series of patches (red windows in A) including tumors are cropped from each slice in A. (C). Series of sub-shells derived from adjacent two patches in B. (D). Shell feature, with grayscale image left and Heatmap image right.

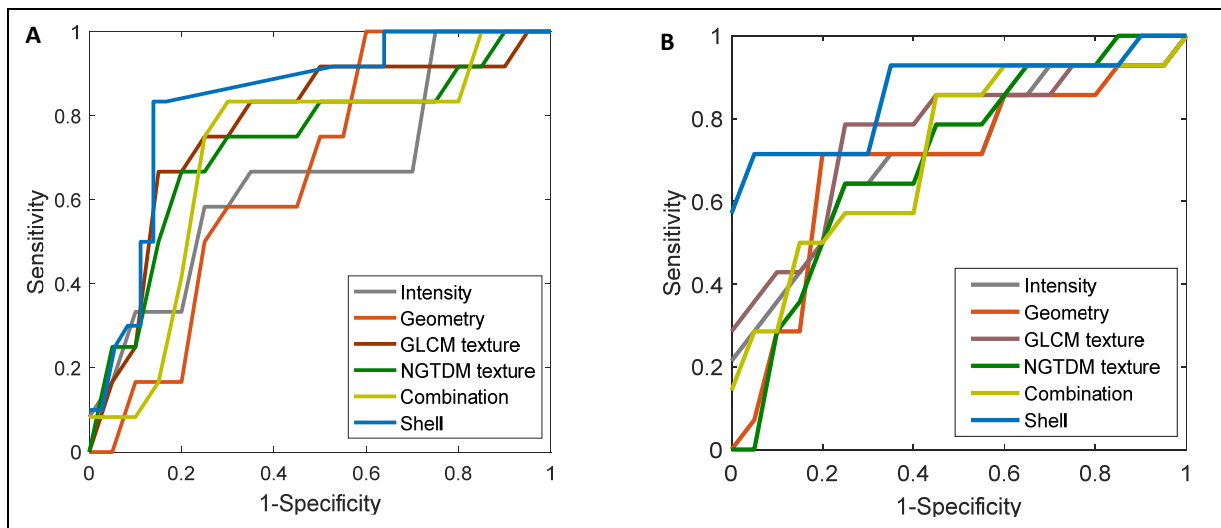


Fig 2. Receiver operating characteristic (ROC) curves of shell feature and other five groups of handcrafted features. (A) NSCLC cohort. (B)CC cohort. ROC curves depict the classification ability of the binary SVM model in terms of predictive feature and observed outcome of distant failure under varied discrimination threshold. The x-axis represents the false positive rate and is calculated as (1-specificity). The y-axis represents the true positive rate by sensitivity. A larger area under the curve indicates better prediction.

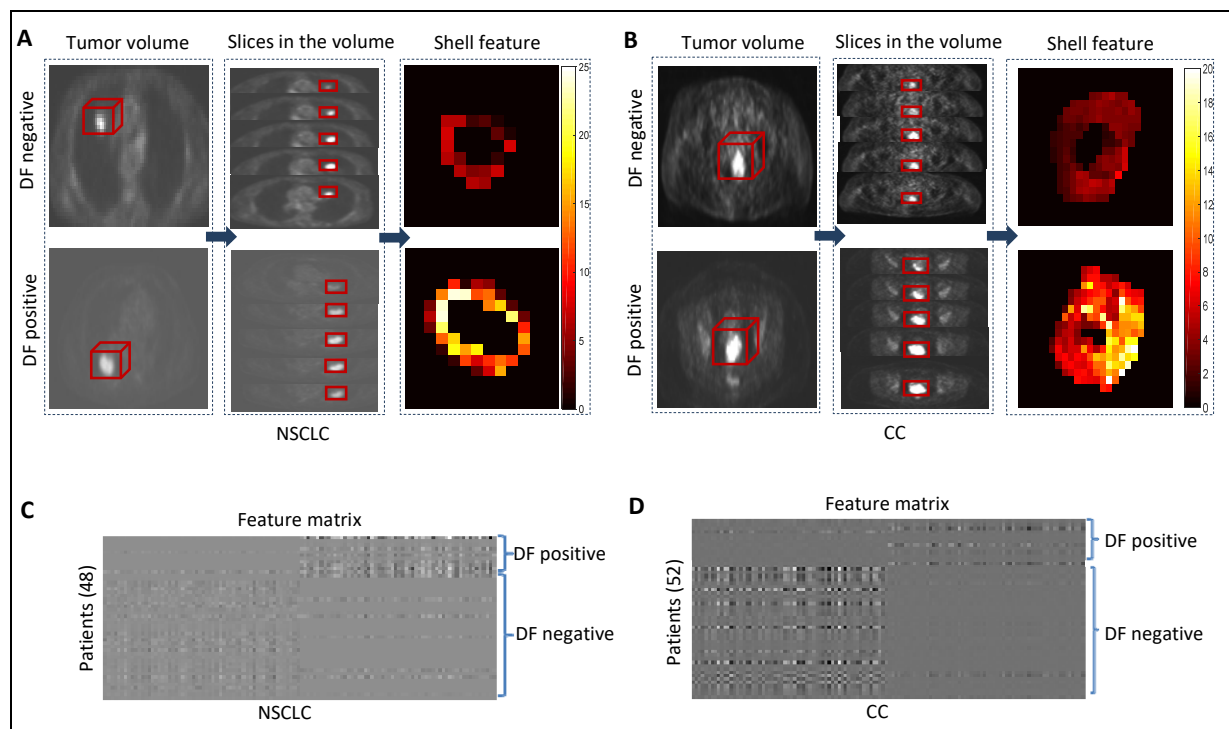


Fig 3. The shell feature has the discriminative ability to detect distant failure (DF)-negative and -positive tumors. (A) (B) are representative examples of 2D shell in terms of structure heterogeneity. (A) NSCLC cases. (B) CC cases. In each cohort, the shell feature (third column) is computed from a series of slices (second column) in the tumor volume (first column), with the top row showing tumors without distant failure and the bottom row showing tumors with distant failure. As shown, tumors with distant failure present more complicated morphologic patterns. (C) (D) are feature matrixes of the whole patients, where each row corresponds to a patient, and each column corresponds to an element of the feature. (C) NSCLC cases. (D) CC cases. These features are sparse coefficients learned from the original vectorized shells by dictionary learning method. These feature matrixes exhibit clustering characteristics for (DF)-positive and -negative tumors.

REFERENCES

1. Steeg PS: Tumor metastasis: mechanistic insights and clinical challenges. *Nature medicine* 12:895, 2006
2. Seyfried TN, Huysentruyt LC: On the origin of cancer metastasis. *Critical reviews in oncogenesis* 18:43, 2013
3. Mehlen P, Puisieux A: Metastasis: a question of life or death. *Nature Reviews Cancer* 6:449-458, 2006
4. Spano D, Heck C, De Antonellis P, et al: Molecular networks that regulate cancer metastasis. *Seminars in cancer biology*, Elsevier, 2012, pp 234-249
5. Chetty IJ, Devpura S, Liu D, et al: Correlation of dose computed using different algorithms with local control following stereotactic ablative radiotherapy (SABR)-based treatment of non-small-cell lung cancer. *Radiotherapy and Oncology* 109:498-504, 2013
6. Timmerman R, Paulus R, Galvin J, et al: Stereotactic body radiation therapy for inoperable early stage lung cancer. *Jama* 303:1070-1076, 2010
7. Nagata Y, Hiraoka M, Shibata T, et al: Prospective trial of stereotactic body radiation therapy for both operable and inoperable T1N0M0 Non-small cell lung cancer: Japan clinical oncology group study JCOG0403. *International Journal of Radiation Oncology* Biology* Physics* 93:989-996, 2015
8. Timmerman R, Hu C, Michalski J, et al: Long-term results of RTOG 0236: a phase II trial of stereotactic body radiation therapy (SBRT) in the treatment of patients with medically inoperable stage I non-small cell lung cancer. *International Journal of Radiation Oncology* Biology* Physics* 90:S30, 2014
9. Zhou Z, Folkert M, Iyengar P, et al: Multi-objective radiomics model for predicting distant failure in lung SBRT. *Physics in Medicine and Biology* 62:4460, 2017
10. Zhou Z, Folkert M, Cannon N, et al: Predicting distant failure in early stage NSCLC treated with SBRT using clinical parameters. *Radiotherapy and Oncology* 119:501-504, 2016
11. Koh W-J, Greer BE, Abu-Rustum NR, et al: Cervical cancer. *Journal of the National Comprehensive Cancer Network* 11:320-343, 2013
12. Whitney CW, Sause W, Bundy BN, et al: Randomized comparison of fluorouracil plus cisplatin versus hydroxyurea as an adjunct to radiation therapy in stage IIB-IVA carcinoma of the cervix with negative para-aortic lymph nodes: a Gynecologic Oncology Group and Southwest Oncology Group study. *Journal of Clinical Oncology* 17:1339-1339, 1999
13. Rose PG, Ali S, Watkins E, et al: Long-term follow-up of a randomized trial comparing concurrent single agent cisplatin, cisplatin-based combination chemotherapy, or hydroxyurea during pelvic irradiation for locally advanced cervical cancer: a Gynecologic Oncology Group Study. *Journal of clinical oncology* 25:2804-2810, 2007
14. Manders D, Kehoe S, Richardson D, et al: Cervical cancer—Distant failure after treatment of para-aortic lymph node metastases. *Gynecologic Oncology* 2:389, 2014
15. Schmid M, Franckena M, Kirchheiner K, et al: Distant metastasis in patients with cervical cancer after primary radiotherapy with or without chemotherapy and image guided adaptive brachytherapy. *Gynecologic oncology* 133:256-262, 2014
16. Joyce JA, Pollard JW: Microenvironmental regulation of metastasis. *Nature Reviews Cancer* 9:239-252, 2009
17. Quail DF, Joyce JA: Microenvironmental regulation of tumor progression and metastasis. *Nature medicine* 19:1423-1437, 2013
18. Wentzensen N, Braumann UD, Einkenkel J, et al: Combined serial section-based 3D reconstruction of cervical carcinoma invasion using H&E/p16INK4a/CD3 alternate staining. *Cytometry Part A* 71:327-333, 2007
19. Braumann U-D, Kuska J-P, Einkenkel J, et al: Three-dimensional reconstruction and quantification of cervical carcinoma invasion fronts from histological serial sections. *IEEE transactions on medical imaging* 24:1286-1307, 2005
20. Wood SL, Pernemalm M, Crosbie PA, et al: The role of the tumor-microenvironment in lung cancer-metastasis and its relationship to potential therapeutic targets. *Cancer treatment reviews* 40:558-566, 2014
21. Bronsert P, Enderle-Ammour K, Bader M, et al: Cancer cell invasion and EMT marker expression: a three-dimensional study of the human cancer-host interface. *The Journal of pathology* 234:410-422, 2014
22. Koelzer VH, Zlobec I, Lugli A: Tumor budding in colorectal cancer—ready for diagnostic practice? *Human pathology* 47:4-19, 2016
23. Koelzer VH, Lugli A: The tumor border configuration of colorectal cancer as a histomorphological prognostic indicator. *Frontiers in oncology* 4:29, 2014
24. Valastyan S, Weinberg RA: Tumor metastasis: molecular insights and evolving paradigms. *Cell* 147:275-292, 2011
25. Chaffer CL, Weinberg RA: A perspective on cancer cell metastasis. *Science* 331:1559-1564, 2011

26. Plaks V, Koopman CD, Werb Z: Circulating tumor cells. *Science* 341:1186-1188, 2013
27. Mani SA, Guo W, Liao M-J, et al: The epithelial-mesenchymal transition generates cells with properties of stem cells. *Cell* 133:704-715, 2008
28. Scheel C, Weinberg RA: Cancer stem cells and epithelial-mesenchymal transition: concepts and molecular links, *Seminars in cancer biology*, Elsevier, 2012, pp 396-403
29. Robertson-Tessi M, Gillies RJ, Gatenby RA, et al: Impact of metabolic heterogeneity on tumor growth, invasion, and treatment outcomes. *Cancer research* 75:1567-1579, 2015
30. Lugli A, Kirsch R, Ajioka Y, et al: Recommendations for reporting tumor budding in colorectal cancer based on the International Tumor Budding Consensus Conference (ITBCC) 2016. *Modern Pathology*, 2017
31. Dawson H, Assarzadegan N, Riddell R, et al: Tumor budding is a strong predictor of disease-free survival in stage II colorectal cancer: Validation study based on the International Tumor Budding Consensus Conference (ITBCC) recommendations, *American Society of Clinical Oncology*, 2017
32. Karamitopoulou E, Zlobec I, Kölzer V, et al: Proposal for a 10-high-power-fields scoring method for the assessment of tumor budding in colorectal cancer. *Modern pathology* 26:295-301, 2013
33. Kadota K, Yeh Y-C, Villena-Vargas J, et al: Tumor budding correlates with the protumor immune microenvironment and is an independent prognostic factor for recurrence of stage I lung adenocarcinoma. *CHEST Journal* 148:711-721, 2015
34. Yamaguchi Y, Ishii G, Kojima M, et al: Histopathologic features of the tumor budding in adenocarcinoma of the lung: tumor budding as an index to predict the potential aggressiveness. *Journal of Thoracic Oncology* 5:1361-1368, 2010
35. Taira T, Ishii G, Nagai K, et al: Characterization of the immunophenotype of the tumor budding and its prognostic implications in squamous cell carcinoma of the lung. *Lung Cancer* 76:423-430, 2012
36. Masuda R, Kijima H, Imamura N, et al: Tumor budding is a significant indicator of a poor prognosis in lung squamous cell carcinoma patients. *Molecular medicine reports* 6:937-943, 2012
37. Huang B, Cai J, Xu X, et al: High-Grade Tumor Budding Stratifies Early-Stage Cervical Cancer with Recurrence Risk. *PloS one* 11:e0166311, 2016
38. Almangush A, Bello IO, Keski-Säntti H, et al: Depth of invasion, tumor budding, and worst pattern of invasion: Prognostic indicators in early-stage oral tongue cancer. *Head & neck* 36:811-818, 2014
39. Rogers AC, Gibbons D, Hanly AM, et al: Prognostic significance of tumor budding in rectal cancer biopsies before neoadjuvant therapy. *Modern Pathology* 27:156-162, 2014
40. Lee H, Chae S, Lee Y, et al: Prognostic implications of type and density of tumour-infiltrating lymphocytes in gastric cancer. *British journal of cancer* 99:1704-1711, 2008
41. Liang F, Cao W, Wang Y, et al: The prognostic value of tumor budding in invasive breast cancer. *Pathology-Research and Practice* 209:269-275, 2013
42. Grigore AD, Jolly MK, Jia D, et al: Tumor Budding: The Name is EMT. Partial EMT. *Journal of clinical medicine* 5:51, 2016
43. Li H, Xu F, Li S, et al: The tumor microenvironment: an irreplaceable element of tumor budding and epithelial-mesenchymal transition-mediated cancer metastasis. *Cell adhesion & migration* 10:434-446, 2016
44. Kadota K, Nitadori J-i, Woo KM, et al: Comprehensive pathological analyses in lung squamous cell carcinoma: single cell invasion, nuclear diameter, and tumor budding are independent prognostic factors for worse outcomes. *Journal of Thoracic Oncology* 9:1126-1139, 2014
45. Betge J, Kornprat P, Pollheimer MJ, et al: Tumor budding is an independent predictor of outcome in AJCC/UICC stage II colorectal cancer. *Annals of surgical oncology* 19:3706-3712, 2012
46. Onozato ML, Klepeis VE, Yagi Y, et al: A role of three-dimensional (3D)-reconstruction in the classification of lung adenocarcinoma. *Analytical Cellular Pathology* 35:79-84, 2012
47. Onozato ML, Kovach AE, Yeap BY, et al: Tumor islands in resected early stage lung adenocarcinomas are associated with unique clinicopathological and molecular characteristics and worse prognosis. *The American journal of surgical pathology* 37:287, 2013
48. Lu S, Tan KS, Kadota K, et al: Spread through Air Spaces (STAS) Is an Independent Predictor of Recurrence and Lung Cancer-Specific Death in Squamous Cell Carcinoma. *Journal of Thoracic Oncology* 12:223-234, 2017
49. Shiono S, Yanagawa N: Spread through air spaces is a predictive factor of recurrence and a prognostic factor in stage I lung adenocarcinoma. *Interactive CardioVascular and Thoracic Surgery:ivw*211, 2016
50. Kadota K, Nitadori J-i, Sima CS, et al: Tumor spread through air spaces is an important pattern of invasion and impacts the frequency and location of recurrences after limited resection for small stage I lung adenocarcinomas. *Journal of Thoracic Oncology* 10:806-814, 2015

51. Travis WD, Brambilla E, Nicholson AG, et al: The 2015 World Health Organization classification of lung tumors: impact of genetic, clinical and radiologic advances since the 2004 classification. *Journal of Thoracic Oncology* 10:1243-1260, 2015
52. Aerts HJ, Velazquez ER, Leijenaar RT, et al: Decoding tumour phenotype by noninvasive imaging using a quantitative radiomics approach. *Nature communications* 5, 2014
53. Cook GJ, Siddique M, Taylor BP, et al: Radiomics in PET: principles and applications. *Clinical and Translational Imaging* 2:269-276, 2014
54. van Baardwijk A, Bosmans G, van Suylen RJ, et al: Correlation of intra-tumour heterogeneity on 18 F-FDG PET with pathologic features in non-small cell lung cancer: a feasibility study. *Radiotherapy and Oncology* 87:55-58, 2008
55. Vriens D, Disselhorst JA, Oyen WJ, et al: Quantitative assessment of heterogeneity in tumor metabolism using FDG-PET. *International Journal of Radiation Oncology* Biology* Physics* 82:e725-e731, 2012
56. Nair VS, Gevaert O, Davidzon G, et al: Prognostic PET 18F-FDG uptake imaging features are associated with major oncogenomic alterations in patients with resected non-small cell lung cancer. *Cancer research* 72:3725-3734, 2012
57. Wu J, Aguilera T, Shultz D, et al: Early-Stage Non-Small Cell Lung Cancer: Quantitative Imaging Characteristics of 18F Fluorodeoxyglucose PET/CT Allow Prediction of Distant Metastasis. *Radiology* 281:270-278, 2016
58. de Geus-Oei LF, van der Heijden HF, Corstens FH, et al: Predictive and prognostic value of FDG-PET in nonsmall-cell lung cancer. *Cancer* 110:1654-1664, 2007
59. Usmanij EA, de Geus-Oei L-F, Troost EG, et al: 18F-FDG PET Early Response Evaluation of Locally Advanced Non-Small Cell Lung Cancer Treated with Concomitant Chemoradiotherapy. *Journal of Nuclear Medicine* 54:1528-1534, 2013
60. Tan S, Kligerman S, Chen W, et al: Spatial-temporal [18 F] FDG-PET features for predicting pathologic response of esophageal cancer to neoadjuvant chemoradiation therapy. *International Journal of Radiation Oncology* Biology* Physics* 85:1375-1382, 2013
61. Nogami Y, Iida M, Banno K, et al: Application of FDG-PET in cervical cancer and endometrial cancer: utility and future prospects. *Anticancer research* 34:585-592, 2014
62. Kidd EA, Siegel BA, Dehdashti F, et al: Clinical outcomes of definitive intensity-modulated radiation therapy with fluorodeoxyglucose-positron emission tomography simulation in patients with locally advanced cervical cancer. *International Journal of Radiation Oncology* Biology* Physics* 77:1085-1091, 2010
63. Mi H, Petitjean C, Dubray B, et al: Robust feature selection to predict tumor treatment outcome. *Artificial intelligence in medicine* 64:195-204, 2015
64. Tixier F, Le Rest CC, Hatt M, et al: Intratumor heterogeneity characterized by textural features on baseline 18F-FDG PET images predicts response to concomitant radiochemotherapy in esophageal cancer. *Journal of Nuclear Medicine* 52:369-378, 2011
65. Schinagl DA, Span PN, Oyen WJ, et al: Can FDG PET predict radiation treatment outcome in head and neck cancer? Results of a prospective study. *European journal of nuclear medicine and molecular imaging* 38:1449-1458, 2011
66. Zhou Z-G, Liu F, Jiao L-C, et al: Object information based interactive segmentation for fatty tissue extraction. *Computers in biology and medicine* 43:1462-1470, 2013
67. Otsu N: A threshold selection method from gray-level histograms. *IEEE transactions on systems, man, and cybernetics* 9:62-66, 1979
68. Gu S, Zhang L, Zuo W, et al: Projective dictionary pair learning for pattern classification, *Advances in Neural Information Processing Systems*, 2014, pp 793-801
69. Bissell MJ, Hines WC: Why don't we get more cancer? A proposed role of the microenvironment in restraining cancer progression. *Nature medicine* 17:320-329, 2011
70. Mezheyski A, Hrynchuk I, Karlberg M, et al: Image analysis-derived metrics of histomorphological complexity predicts prognosis and treatment response in stage II-III colon cancer. *Scientific reports* 6, 2016
71. Lennon FE, Cianci GC, Cipriani NA, et al: Lung cancer [mdash] a fractal viewpoint. *Nature Reviews Clinical Oncology* 12:664-675, 2015